Ice Flow in the Humboldt, Petermann, and Ryder Glaciers, North Greenland

Ian Joughin

Mark Fahnestock

Ron Kwok

Prasad Gogineni

Chris Allen

ABSTRACT

Radar interferometry, ice-penetrating radar profiles, and an elevation model are used to determine the catchment areas, rates of ice discharge, and approximate states of balance for three large outlet glaciers in northeast Greenland. Discharge through several flux gates is calculated for the Humboldt and Petermann glaciers, which are found to be in balance (at the level that accumulation is known) if modifications are made to ablation parameterization. The Ryder appears to require that there be large errors in the accumulation data for it to be in balance, but this may be a reflection of the unsteady flow behavior of this glacier. The patterns of ice flow for the three glaciers considered are each unique, showing that the nature of ice discharge varies substantially from basin to basin, controlled by bed conditions and the presence of sub-glacial troughs and obstructions.

INTRODUCTION

Much of the annual mass loss of the Greenland ice sheet is through outlet glacier discharge. In northern Greenland, where surface ablation rates are much smaller than in the south, ice discharge is the dominant form of mass wastage. Recent results by Rignot and others [1997] have demonstrated that discharge in northern Greenland is roughly 3.5 times greater than previous estimates. The discrepancy with earlier estimates can be attributed to differences between the direct measurement of ice discharge at the grounding line verses estimates derived from calving rates, which were biased low because of unexpectedly high basal melt rates [Rignot and others, 1997]. In this paper we use recently derived satellite radar interferometry techniques in conjunction with ice-sounding radar data to examine the discharge and dynamics of three of the larger outlet glaciers that drain the northern sector of the Greenland ice sheet.

The study of ice discharge has been hindered by a lack of data. Even with the advent of the global positioning system (GPS), ground based surveys are expensive, logistically-difficult, and provide measurements at only a limited number of points. Tracking of features in pairs of visible (Scambos and others, 1992; Ferrigno and others, 1993) or synthetic aperture radar (SAR) images (Fahnestock and others, 1993) can provide valuable velocity data, but not for the featureless areas found over much of the ice sheets.

Since the launch of the ERS-1 SAR, several researchers [Goldstein and others, 1993; Hartl and others, 1994; Joughin 1995, Joughin and others 1995, 1996abc, 1997; Rignot 1996, Rignot and others, 1995, 1996, 1997; and Kwok and Fahnestock, 1996] have demonstrated that satellite radar interferometry (SRI) is capable of accurately measuring ice velocity and surface topography for even the most featureless areas. As such, SRI represents a powerful new remote-sensing

technique for glaciological study. Currently the main limitations to widespread application of this technique are lack of coverage over certain areas, limited access to existing data-sets, and limited availability of ground control.

In this paper we present interferometrically-derived velocity fields for the Humboldt, Petermann, and Ryder Glaciers in northern Greenland. Our data reveal differing styles of flow for each of these glaciers. The scale of the velocity maps demonstrate that, given adequate coverage, it is feasible to map velocity at high spatial resolution over entire drainages. We have used this data in combination with ice-thickness profiles collected by the University of Kansas Coherent Radar Depth Sounder (CORDS) to estimate discharge fluxes on grounded ice, which we compare with balance fluxes. We also use the bed topography provided by the sounder to aid in interpretation of the dynamics of these glaciers.

BRIEF INTERFEROMETRY BACKGROUND

We give only a brief review of repeat-pass interferometry here as detailed descriptions of the repeat-pass interferometric techniques we use have been given elsewhere [Joughin and others, 1995, 1996ab, in press]. A repeat-pass interferometric SAR images a scene at different times from two nearly repeating orbits, separated by a baseline. An interferogram is formed as the product of the resulting complex SAR images. If the relative phases of the scatterers within a pixel remain the same for each pass, then the phase of the interferogram is non-random and is proportional to the range difference from one pass to the next. In practice, the slight difference in look angles, due to the baseline separation, alters the relative phases of scatterers, causing partial or full decorrelation of the complex images, which has the effect of introducing phase noise. Fur-

ther phase noise is introduced by temporal decorrelation caused by pass-to-pass changes in the relative positions of sub-pixel scatterers (i.e., blowing snow) or other changes that affect the scattering (i.e., melting). Decorrelation also results from system noise, processing errors, and image misregistration.

The phase of an interferogram is a direct measure of the change in line-of-sight range to a pixel from one pass to the next. This range difference is affected by the surface topography with the topographic sensitivity determined by the baseline. With accurate knowledge of the baseline, interferometric phase data can be used to generate high-resolution maps of surface topography (Li and Goldstein, 1990, Zebker and other, 1994).

Surface displacement between passes causes an additional difference in range. The phase of the resulting interferogram provides a measure of the component of displacement that is directed along the radar line-of-sight (Gabriel and others, 1991). Because phase accuracy is much greater than the radar wavelength (λ = 5.6 cm for ERS-1/2) it is possible to measure millimetric displacements from space.

The phase of an interferogram is initially computed modulo-2π, with each phase cycle (fringe) corresponding to a range change of half the radar wavelength ($\lambda/2$ = 2.8 cm for ERS-1/2). Phase-unwrapping algorithms (Goldstein, 1988) are used to remove this modulo-2π ambiguity so that quantitative measurements can be made.

Most interferometric applications require knowledge of the baseline to a level of accuracy beyond that which can be achieved with even the best orbital state vectors. Typically, some form of ground control must be used to solve for the baseline. At least four points of known elevation and displacement are needed to determine the parameters for the baseline when it is modeled as

having a linear along-track variation. An analysis of the impact of baseline accuracy on ice motion measurements has been given by Joughin and others (1996).

An interferogram contains the combined effects of topography and displacement, which must eventually be separated to make motion and topography estimates. This can be achieved fairly easily when two interferograms with different baselines are available (Kwok and Fahnestock, 1996). A full description of the double-difference method we use to separate motion and topographic effects has been given by Joughin and others, 1996a.

Interferograms acquired along a single-track are sensitive only to a single component of displacement as determined by the radar line-of-sight. If the vertical component of displacement is ignored or at least partially compensated for using surface-slope information (Joughin and others, 1996b), then one component of the horizontal velocity vector can be estimated. Flow direction can be estimated from the direction of maximum averaged (i.e., over scales of several ice thicknesses) downhill slope (Paterson, 1994) although with poor spatial resolution. The horizontal velocity vector can then be determined using the single measured horizontal component and the estimated flow direction. This method can yield reasonable estimates when the flow is in a direction where there is a reasonable sensitivity to motion (i.e., the flow direction is not too different from the radar line-of-sight).

In principle, direct measurement of the full three-component velocity vector requires data collected along three different satellite-track headings. Collection of such data is not possible with existing SARs. With the assumption that ice flow is parallel to the ice-sheet surface, however, it is possible to determine the full three-component velocity vector using data acquired from only two directions and knowledge of the surface topography (Joughin and others, in press;

Mohr and others, submitted). Using this assumption, small deviations from surface-parallel flow (i.e., the submergence and emergence velocity) are ignored, which is of limited consequence for many glaciological studies. These variations from surface-parallel flow, however, do contain information on local thickening and thinning rates. Thus, an interferometer that allows collection of data from three directions would be useful for studying mass balance and interpreting altimeter-derived thickening and thinning rates.

STUDY AREA AND DATA SOURCES

The area containing the drainages of the Humboldt, Petermann, and Ryder glaciers is shown in Figure 2. The imagery in this figure is taken from an ERS-1 SAR mosaic of Greenland (Fahnestock and others, 1993). The boundaries of the drainage divides (shown in white) were mapped using standard methods (Bindschadler, 1984) applied to the National Survey and Cadastre (KMS) digital elevation model (DEM) (Ekholm and others, 1996), which we have plotted over the imagery at 100-m contour levels (green). The locations of the CORDS ice-thickness profiles are shown in red, and the places where we have interferometric data are illustrated with yellow rectangles. Finally, we have plotted balance velocities for the area where the nominal ice thickness is greater than 500 m. These velocities were computed with the algorithm used by Joughin and others (1997) in an earlier study, but modified here to include an ablation model to allow computation of balance velocities at lower elevations, where significant melting takes place.

The Humboldt differs from the Petermann and Ryder in that it has a much broader calving front (greater than 100 km), which is grounded for most of its extent. Because of its width, the Humboldt flow is only weakly convergent near the terminus. In contrast, the Petermann and

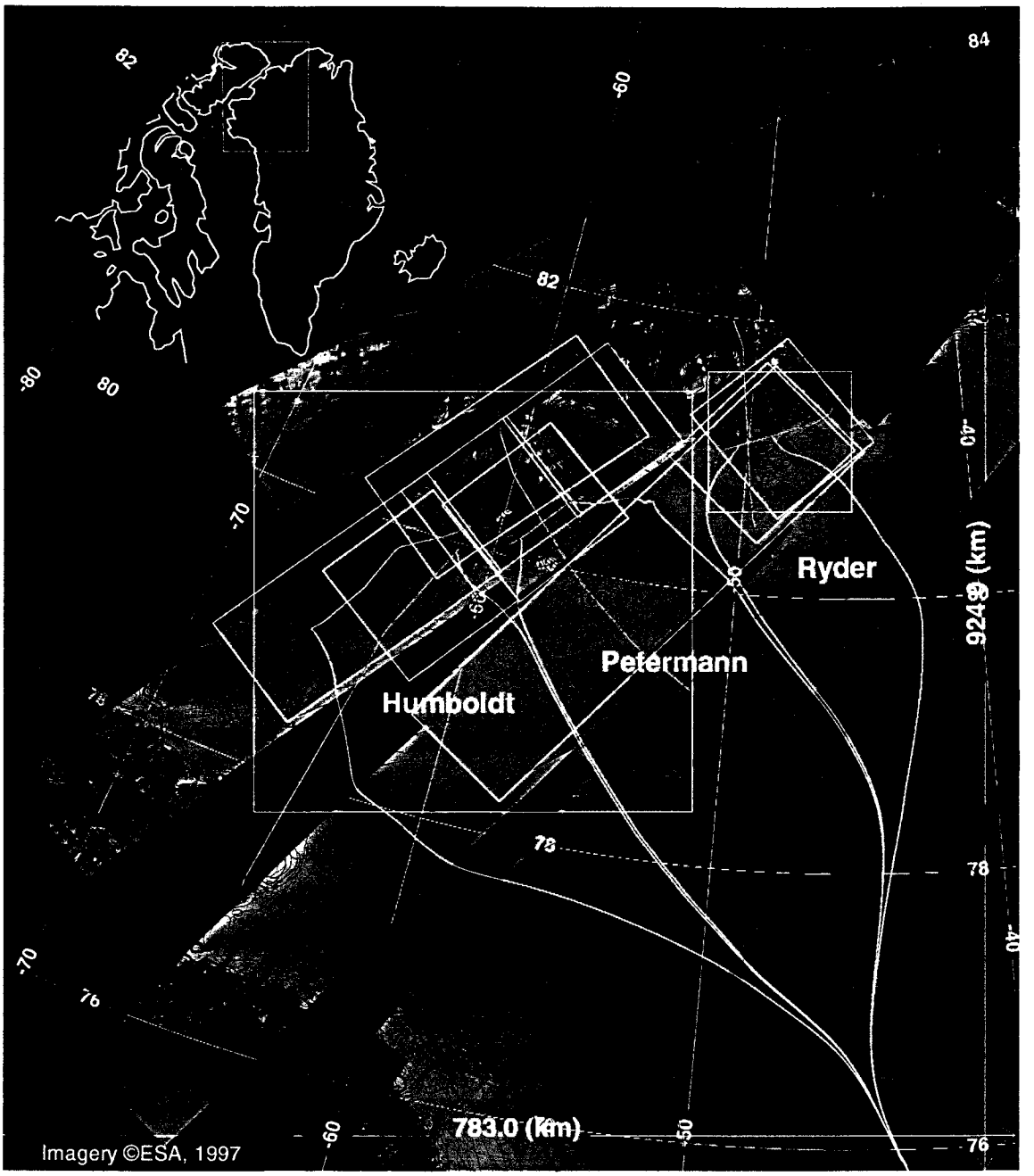

Figure 1. ERS-1 SAR imagery of NW Greenland showing the drainages (delineated by white lines) of the Humboldt, Petermann, and Ryder Glaciers. KMS DEM contours at 100-m intervals are plotted in green. Balance velocities are plotted with 20 m/yr cyan contours for velocities up to 180 m/yr and with dark-blue 100 m/yr contours. Locations of images used for interferometry are indicated with yellow rectangles and CORDS flight lines are plotted in red. The white rectangles show the locations of subsequent figures.

Ryder are much narrower, have highly convergent flow patterns upstream of their respective fiords, and terminate in relatively long, floating ice tongues. While the Petermann and Ryder are similar in these aspects, the Petermann has a catchment that is more than twice as large as that of the Ryder (Table 2). The balance velocities indicate that the enhanced flow of the Petermann extends well into the ice sheet, indicating that the fiord likely exists as a channel well back under the ice sheet. The onset of rapid flow is found much nearer the coast for the Ryder, with two distinct branches that merge as ice enters the exposed confines of the fiord. This glacier has recently exhibited mini-surge behavior (Joughin and others, 1996c), whereas no flow instabilities have been documented for the Petermann or Humboldt.

The interferometric data used in this study were all acquired with the European Space agency's ERS-1 and ERS-2 SARs. To minimize temporal decorrelation from surface melt, all of the data we used were acquired in the months of September through March. The dates, orbits, and frames of the SAR data used in this study are identified in Table 1. Most of the interferometric pairs were acquired during periods when ERS-1 was flying in a 3-day repeat cycle. For rapidly moving areas (i.e., greater than a few hundred m/yr) the 3-day data were difficult to unwrap because of strong gradients in the phase. To estimate velocity in these regions, we used ERS-1/2 tandem data. During the tandem mission, the orbit of ERS-2 lagged that of ERS-1 by one day to allow collection of one-day interferometric pairs, using one image from each SAR.

We ordered the raw SAR signal data, which we processed to form the single-look complex (SLC) images used to create interferograms. From the interferometric data we computed our elevation and velocity estimates. Details of the techniques used to derive these estimates have been

Table 1. Humboldt, Petermann, and Ryder interferograms.

SARs	Orbits	Frames	Dates	B_n (m)
E1/E1	1743/1786	1953	November 15 & 18, 1991	117
E1/E1	2904/2947	1935-1989	February 4 & 7, 1992	228
E1/E1	2947/2990	1935-1989	February 7 & 10, 1992	-2
E1/E1	3248/3291	1953	February 28 & March 2, 1992	-5
E1/E1	3477/3520	1935-1989	March 15 & 18, 1992	-60
E1/E1	3520/3563	1935-1989	March 18 & 21, 1992	164
E1/E2	22416/2743	1935-1953	October 28 & 29, 1996	-17
E1/E2	21886/2213	1935	September 21 & 22, 1996	41
E1/E2	22387/2714	1935	October 26 & 27, 1996	94
E1/E2	22577/2904	1665	November 8 & 9, 1996	94
E1/E2	23579/3906	1665	January 17&18, 1996	195
E1/E2	23332/3659	1971	December 31, 1995 & January 1, 1996	-24
E1/E2	23833/4160	1971	February 4 & 5, 1996	197

given by Joughin and others (1996ab, and in press).

Elevation data were needed to provide control points for the baseline estimation. We extracted our control points from the KMS DEM for northern Greenland (above 78°). This elevation model (Ekholm and others, 1996) was derived from GEOSAT and ERS-1 satellite altimetry, GAP airborne altimetry, local survey, and coastal elevations, which were derived from photogrammetry. Airborne altimetry data was used in the production of the DEM to reduce long-wavelength errors in the satellite altimetry along the sloping sides of the ice sheet.

The ice-thickness measurements were acquired with the University of Kansas CORDS

instrument. This system (Chuah and others, 1996) is an improved version of an original system that has been described by Raju and others (1990). The system was operated from a NASA P-3 aircraft that was also equipped with precision laser altimeter systems and Global Positioning System (GPS) receivers. Consequently, the radar data are tagged with precise GPS location information, providing accurate registration of sounding data with sensor position and an independent measurement of the ice surface elevation.

The coherent radar system operates at a center frequency of 150 Mhz with a nominal pulse-repetition frequency (PRF) of 9800 Hz. The transmitter generates a pulse that is frequency modulated (chirped) over a bandwidth of 17 MHz with a duration of 1.6 microseconds and a peak power of 200 W. Separate transmit and receive antennae, each a four-element dipole array, are mounted beneath the left and right wings. The receiver, protected during transmit events by a blanking switch, amplifies and compresses the received signal in a weighted SAW compressor resulting in a compressed pulse length of about 60 ns and a depth resolution of 5 m in ice (n = 1.78). The end-to-end receiver gain is about 95 dB. The compressed signal is coherently detected, providing in-phase and quadrature (I and Q) analog outputs. Two 8-bit A/D converters, with a sampling rate of 18.75 megasamples/sec (MSPS), are used to digitize these analog signals. Coherent integration is then performed by summing complex data vectors from 256 consecutive transmit-receive periods. The power (i.e., $I^2 + Q^2$) for each of these averages is computed and incoherently integrated by summing four consecutive samples.

The two-way antenna, half-power beamwidths are about 18 and 66 degrees in the planes perpendicular and parallel to the flight path, respectively. The coherent integration serves as a low-pass filter on the data and reduces the along-track antenna beamwidth from about 66 to 7

degrees at the nominal velocity of 110 m/s. We believe the pulse compression, coherent processing and the bistatic antenna arrangement allowed this system to succeed in sounding outlet glaciers.

VELOCITY FIELDS

Humboldt/Petermann

Figure 2 shows the interferometrically-derived across-track velocity field for the area enclosed by the large white rectangle in Figure 2. We have also produced an accompanying DEM (not shown), which was used to remove the effects of height and slope in making the velocity estimates. A portion of this map containing the Humboldt was published earlier by Joughin and others (1996b). We have since improved and expanded the Humboldt results through the inclusion of additional data. Where there are SAR data, breaks in the contours correspond to areas where we could not make estimates because of problems unwrapping the phase. We did not estimate velocities on the floating ice tongue because additional data are needed to remove the effect of tidal displacement. Interferometric estimates of velocity on the floating ice tongue have been published by Rignot (1996).

The satellite tracks are not quite parallel, so the across-track direction is slightly different for each strip. These differences are minor, however, as is apparent from the smooth transition of contours from swath to swath. We have estimated the flow direction using the KMS DEM, which we illustrate with magenta arrows in Figure 2. The flow direction is nearly aligned with the across-track direction over most areas so that the across-track component of velocity is represen-

tative of ice-flow speed. In subsequent plots and for flux calculations we use the horizontal velocity vector computed using the across-track velocity and estimated direction of flow.

The Humboldt reaches peak speeds of about 440 m/yr along the portion of its calving face just to the southwest of the area that juts out. Near this area there is a bright region in the SAR imagery, which we attribute to the presence of small icebergs acting as strong radar reflectors.

The Petermann, with a greater overall discharge and narrower outlet, achieves speeds of over 1100 m/yr at the grounding line. A rapid increase in speed is seen where the glacier narrows significantly as it enters the fiord. Qualitatively the contours for both glaciers shown in Figure 2 agree well with the corresponding balance velocities of Figure 1. In particular, the balance velocities provide a good prediction of the location where rapid flow begins on the Petermann.

Errors arise from a number of sources including errors in the baseline, phase noise due to decorrelation, varying propagation delay due to atmospheric anomalies, other anomalies in the SAR data, and errors in the interferometric DEM used to correct for topography and slope effects. A more detailed discussion of these errors has been given by Joughin and others (1996b). Some of the error sources, atmospheric artifacts in particular, still are not well characterized for polar regions.

We do not have independent velocity estimates on the ice sheet to compare with our results. The standard deviation of the velocity estimates on the stationary, ice-free area is 2.4 m/yr. Since the control points were taken from the ice-free area, the error should be slightly lower in this region. A reasonable estimate for the level of error on the ice sheet is 5 m/yr. Because the velocity map is compiled from several independently derived estimates, the errors may be slightly higher for some strips and lower for others.

We did encounter problems in processing the strip furthest inland (lower right) in Figure 2. The baseline for this strip was originally estimated with control points from the adjacent ice-free area, which was sufficient for the other strips. With the inland strip, however, we obtained initial results with negative (uphill) velocities as high as -118 m/yr. This large error can be attributed to the small size of the patch of data over which we had control points (not shown in Figure 2) and the need to extend the baseline estimate nearly 400 km from this region. The ideal way to overcome this problem would be to use control points with velocity and elevation measured on the ice sheet near the upper end of the strip. Since we did not have such data available to us, we resorted to using balance velocities as control points at the locations indicated by white "+" symbols in Figure 2. The ice flows at about 20 m/yr in this region. Even with errors of 50% in balance velocities, the absolute errors in the control points would only amount to 10 m/yr. Errors this large would have the effect of introducing a systematic error over the image in the form of a nearly linear ramp with a deviation of about 10 m/yr over the 400 km scene. One indication that the balance velocities provided reasonable control is that the velocity measured with GPS at the nearby Humboldt Camp (K. Steffen, personal communication) seems consistent with our velocity map (Figure 2). While not an ideal solution, the use of balance velocities improved our results significantly for this strip. Furthermore, since none of the CORDS profiles cross this strip, our flux estimates are not affected by the use of these balance-velocity-derived control points.

Ryder

We were fortunate enough to have coverage from both ascending and descending orbits (i.e., coverage from two directions) for the Ryder, which allowed us to determine the three-dimen-

sional velocity field under the surface-parallel-flow assumption. These data were used earlier for the initial demonstration of the three-dimensional velocity technique (Joughin and others, in press). The resulting horizontal velocity field for the Ryder is shown in Figure 3. The data reveal the two branches of the Ryder, which converge at an elevation of 1000 m and then flow out through the fiord. At higher elevations the regions of converging flow associated with each of the two branches are visible, while further downstream the shear margins of the two branches become more distinct. In places where there are flow stripes or other indicators of flow direction, there is good agreement with the measured flow direction. As the ice enters the fiord, flow is shunted to the west by what is likely a bedrock obstacle. There also appears to be a subglacial ridge running across the entrance to the fiord. Behind this ridge there is an ice plain with several supraglacial lakes that show up as bright areas in the SAR imagery. Once ice enters the fiord, the flow becomes more evenly distributed across the fiord.

When combining ascending and descending data it is assumed that ice flows at the same rate during the acquisition of both interferometric pairs. Usually this is a reasonable assumption for ice sheets and outlet glaciers, especially if the data are all acquired in winter. Joughin (1995) and Kwok and Fahnestock (1996) have observed steady flow rates for periods ranging from days up to nearly two years. The Ryder, however, varies its speed. A mini-surge occurred sometime in the interval from September 22 through November 8, 1995 (Joughin and others, 1996c). During this event, the speed on parts of the glacier appears to have increased by more than a factor of three over the normal rate. The results shown in Figure 3 were generated using descending data that were acquired before the mini-surge and ascending data acquired afterwards. While the Ryder

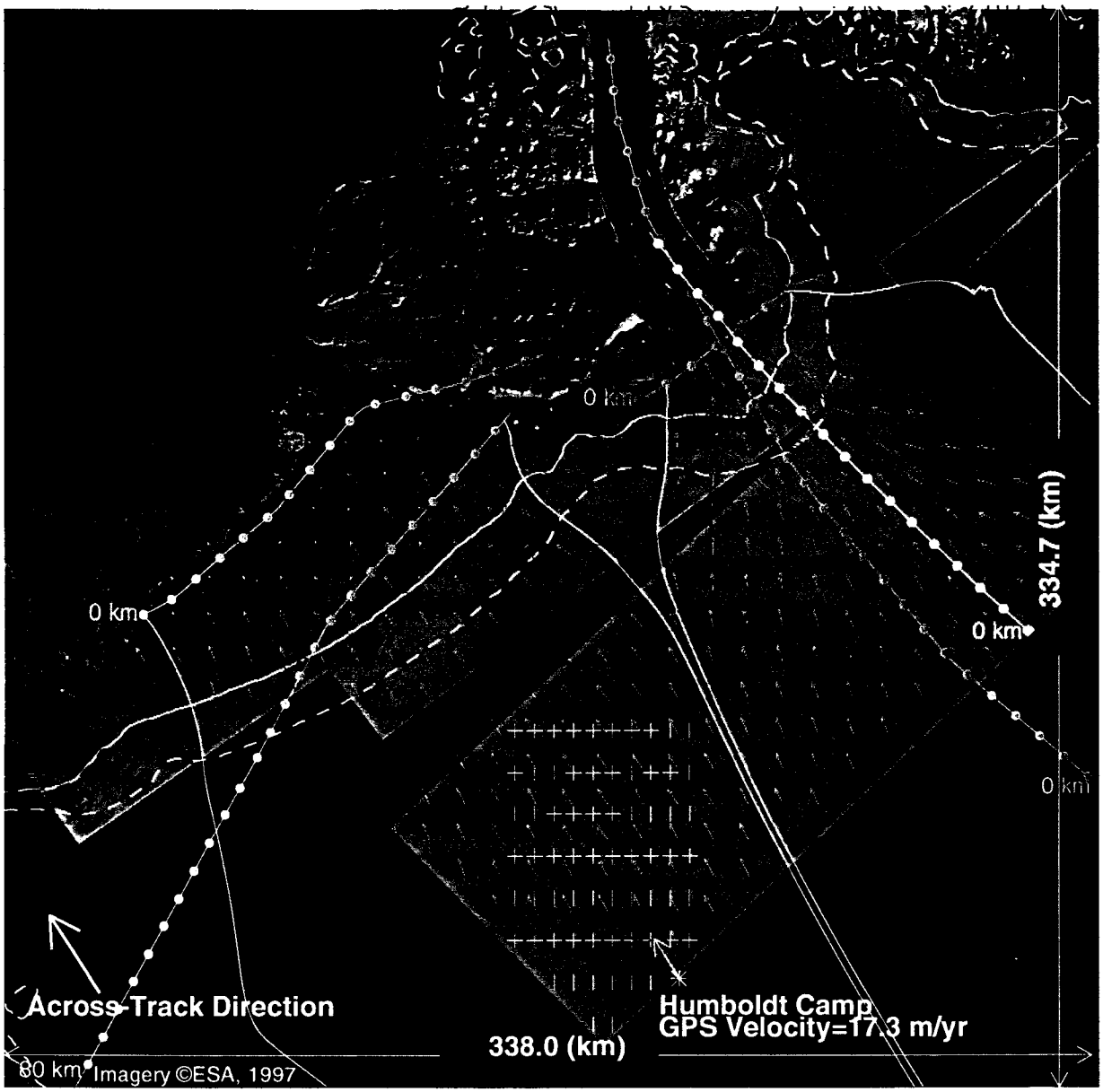

Figure 2. Contour map of the across-track component of velocity for the Petermann and Humboldt corresponding to the area indicated by the large white rectangle in Figure 1. The approximate across-track direction is indicated by an arrow in the lower left corner. Flow direction estimated from the KMS DEM is shown with magenta arrows. The across-track velocity is shown with 20 m/yr cyan contours for velocities up to 180 m/yr and with dark-blue 100 m/yr contours. CORDS profiles are shown in red, and the centerline of the Petermann is in yellow. These lines are marked with dots at 10-km intervals. Orange lines show the snow (solid) and runoff (dashed) lines predicted by the degree-day ablation model while the corresponding lines are shown in blue for the rescaled ablation model (see text).

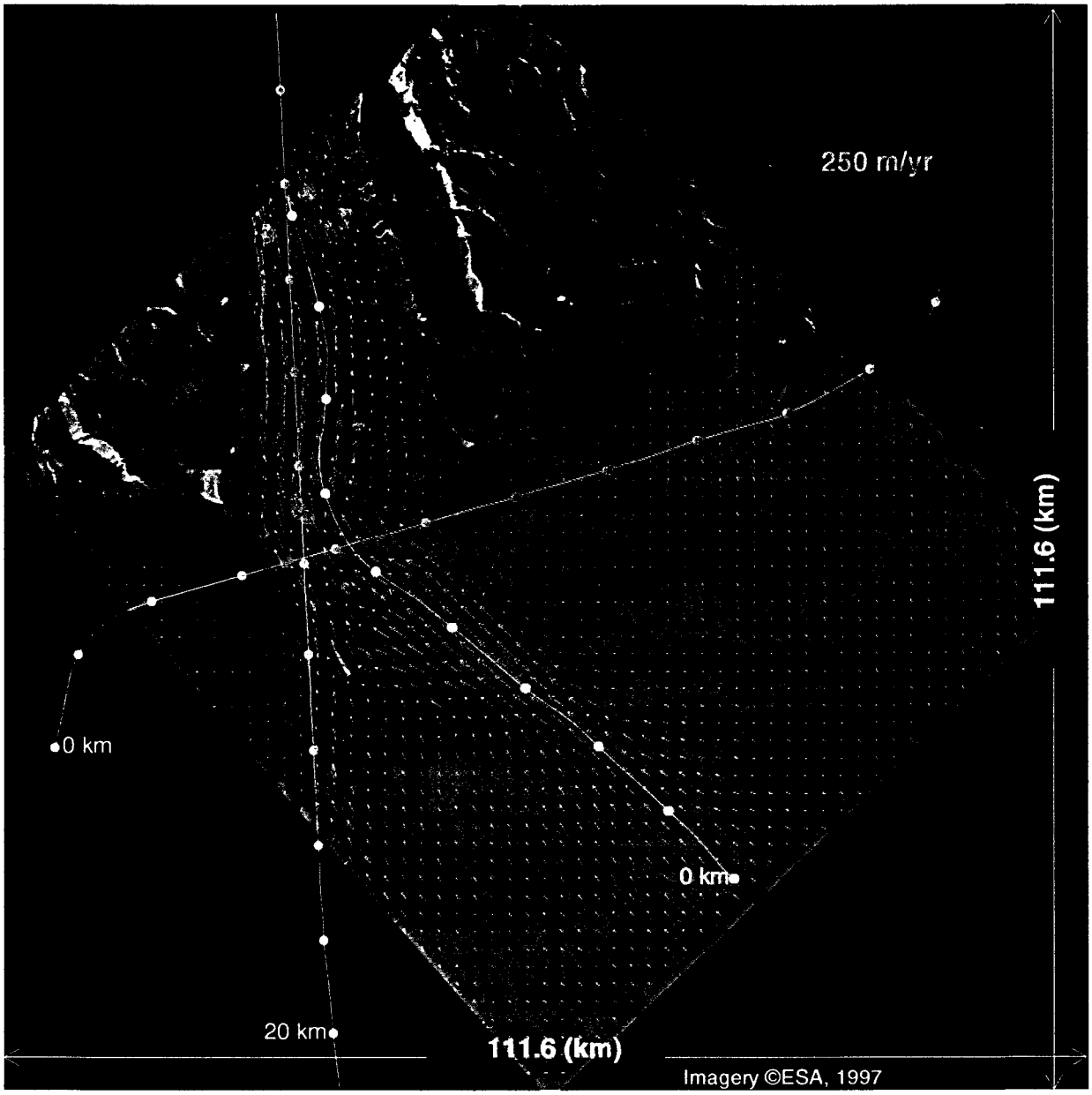

Figure 3. Horizontal velocity field for the Ryder Glacier. The speed is shown with 20 m/yr cyan contours for speeds up to 180 m/yr and with dark-blue 100 m/yr contours. Velocity is plotted as a vector field with magenta arrows. The red profiles correspond to CORDS data, while the yellow profile corresponds to a flowline. Dots are used to mark 10 km intervals along the profiles.

appears to have been in a mode of steady flow during these acquisitions, there may be differences in the flow rates observed during descending and ascending acquisitions. From our analysis of the data, we believe that any such differences are small (i.e., the directions of the flow vectors agree well with flowlines visible in the SAR imagery).

All of the errors that affect single component estimates of velocity (i.e., Figure 2) also affect estimates made using ascending and descending passes. Misregistration of the ascending and descending data is an additional source of error. Error analysis is complicated by the fact that the data are combined in a spatially varying way that is dependent on slope. A more detailed discussion of these sources of error has been given by Joughin and others (in press). Rather than estimating error by tabulating the individual sources of error, the magnitudes of which may be unknown, we take the same approach as we did for the Humboldt/Petermann data and examine the velocity in the ice-free areas. The standard deviation of the velocity on the ice-free areas is 4.7 m/yr. Allowing for additional baseline error away from the ice-free control areas we roughly estimate the magnitude of error for our velocity estimates to be 7 m/yr. Further research is needed to improve error estimates for interferometric ice flow measurements.

DISCHARGE ESTIMATES

Profile Data

Ice-thickness data have been collected with the CORDS instrument at the locations shown in Figure 1; these profiles are shown again for the Humboldt and Petermann in Figure 2 and for the Ryder in Figure 3. Four of these profiles run across the outlets, making them suitable for dis-

charge estimates. The bed and surface topography along these profiles are shown in Figure 4 along with the component of velocity normal to the gate and the magnitude of the velocity. The bed topography in this figure was determined by subtracting the CORDS ice-thickness estimates from the interferometrically determined surface topography. Figure 4a indicates that ice thickness in the Humboldt channel along the profile nearest the coast ranges from roughly 300-600 m. Thickness is more uniform along the inland profile, with an average depth of 875 m. The channel does not have a well defined wall along its southwestern edge. In contrast, both Humboldt profiles show a steep wall several hundred meters high forming the northeastern boundary of the channel. The bed along both Humboldt profiles has several notches with widths of a few kilometers and depths of a few hundred meters. There are several corresponding peaks in the coastal velocity profile, perhaps indicating that the subsurface features represent small sub-channels within the channel. At the inland profile flow is more regular, with only the deepest subsurface feature corresponding to enhanced flow.

The profile across the Petermann channel, which is shown in Figure 4, indicates that the Petermann has a far more well defined channel than that of the Humboldt. At a width of about 40 km, the Petermann channel is significantly narrower than Humboldt's and is bounded on either side by steep walls of 600-800 meters in height. The elevation of the channel bed ranges from 200 to 400 m below sea level, with the deepest portion corresponding to the section of fastest flow. The profile shows a small secondary channel at about 53 km, which from the velocity map (Figure 2) appears to merge with the main channel a few kilometers downstream. The surface topography profile has a dip of about 100 m over the channel and a steep slope at 48 km above

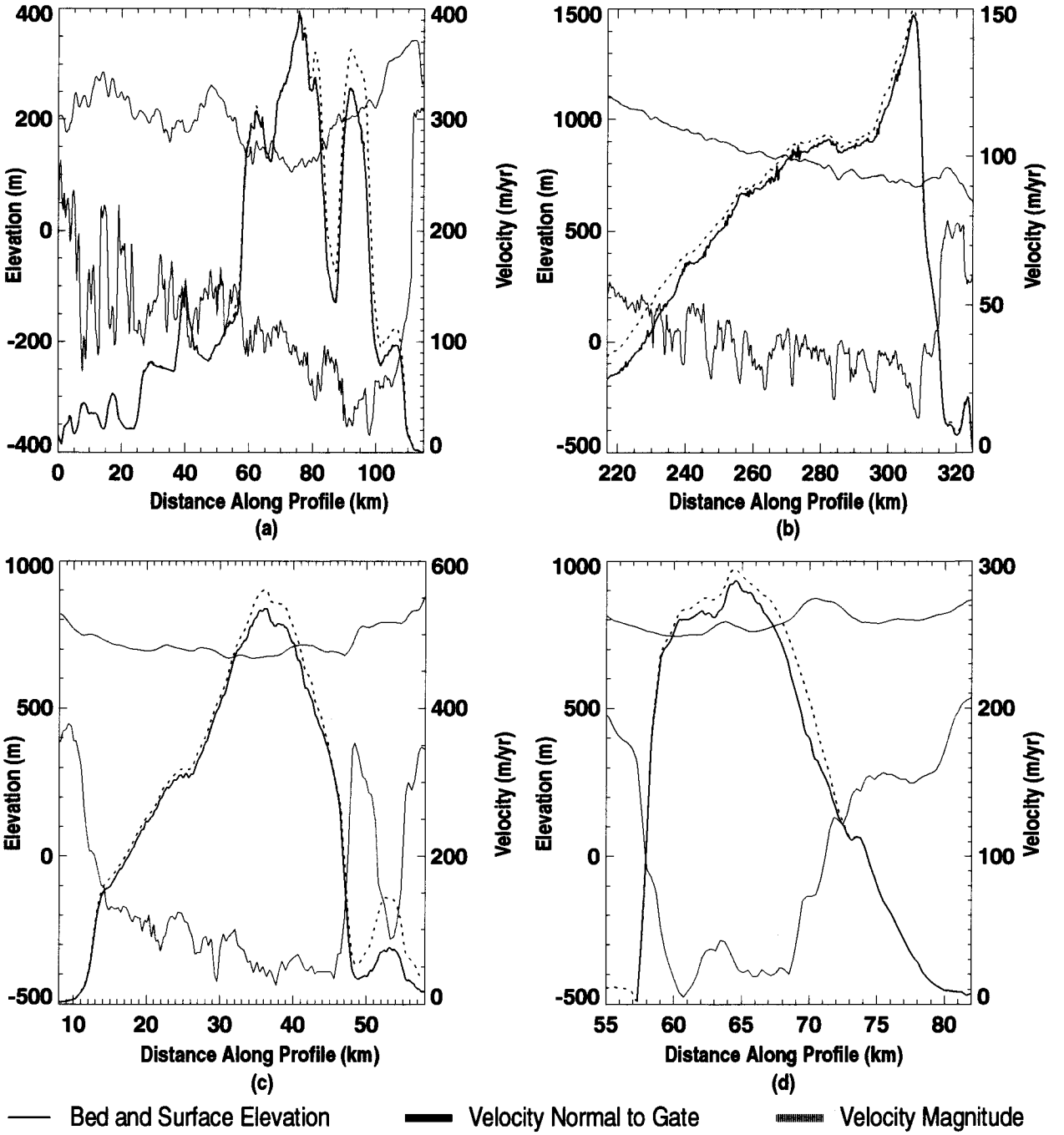

Figure 4. Transverse profiles used in flux calculations for (a) Humboldt coast, (b) Humboldt inland, (c) Petermann, and (d) Ryder. Bed elevations were determined by subtracting CORDS ice-thickness data from interferometrically-derived height data. For Humboldt and Petermann the velocity vector was determined using the across-track component and the flow direction estimated from the KMS DEM.

the channel wall.

With a width of approximately 17 km, the Ryder has the narrowest channel of the three glaciers discussed in this paper. The depth and the height of the channel walls are comparable to those of the Petermann. The 100-m scale bump in the bed at around 63 km is probably the last remaining separation between what are far more distinct channels further upstream. As with the Petermann and Humboldt, features in the bed topography are evident in the surface profile.

Flux Measurements and Analysis

We used the data shown in Figure 4 to measure discharge fluxes, which are listed in Table 2. In making these estimates, we subtracted a value of 12 m from the thickness data to account for the lower density of the firn layer (Alley and Bentley, 1988). We assumed that most of the motion was due to sliding so that the depth-averaged velocity is equal to the surface velocity. We were only able to estimate flux for the portion of the inland Humboldt profile where we have velocity data (Figure 2). The green flowline shown in Figure 2 extends from the last point of this profile for which we have velocity data to the coastal profile. To facilitate comparison with the inland profile, we also estimated discharge for the subsection of the coastal profile northeast of the flowline. Table 2 also includes estimates of discharge at the Petermann and Ryder grounding lines made by Rignot (personal communication), which have been revised from values given by Rignot and others (1997).

We used an accumulation map based on the data of Ohmura and Reeh (1991) to estimate the total accumulation upstream of each profile (Table 2). The accumulation map is based on the gridded version of the Ohmura and Reeh (1991) data that was prepared for the European Ice

Table 2. Ice-equivalent discharge fluxes for the Humboldt, Petermann, and Ryder glaciers computed from velocity and ice-thickness data sets. The average accumulation rate and total accumulation rate upstream of each profile are computed from the Ohmura and Reeh (1991) accumulation data. Ablation was estimated with the degree-day model (Reeh). Estimated flux is the difference between estimates of accumulation and ablation.

Profile	Avg. Acc. Rate (mm/yr) w.e.	Area (km^2)	Accumulation (km^3/yr) i.e.	Ablation (km^3/yr) i.e.	Estimated Flux (km^3/yr) i.e.	Measured Flux (km^3/yr) i.e.
Humboldt Inland	208	37,310	8.46	0.35	8.10	7.01±0.44
Humboldt Coast	210	48,106	11.0	4.18	6.82	6.22±0.22
Humboldt Coast (subsection)	207	40,606	9.18	3.44	5.74	5.81±0.17
Petermann Transverse	176	69,894	13.5	0.27	13.2	12.4±0.22
Petermann Grounding Line	177	71,093	13.7	1.70	12.0	12.0*
Ryder Transverse	174	28,553	5.42	0.05	5.37	3.9±0.15
Ryder Grounding Line	174	29,447	5.61	0.92	4.69	2.36*

* from Rignot (personal communication)

Sheet Modeling Intercomparison (EISMINT). We re-interpolated the EISMINT data to the Special Sensor Microwave Imager (SSMI) polar stereographic projection at the resolution used for our data sets.

We estimated the total ablation upstream of the flux gates (Table 2) using the degree-day model of Reeh (1991) with a value 4.5°C for the standard deviation of the temperature. The model was implemented with the temperature parameterization of Huybrechts and others (1991) and with degree-day factors of 0.003 m and 0.008 m of water per degree day for snow and ice,

respectively. We subtracted these ablation estimates from the accumulation data to estimate fluxes above each profile (Table 2).

The estimated flux of the Humboldt inland profile is greater than the measured flux by 1.09 km^3/yr, which suggests a thickening of the ice sheet in the upper accumulation zone. We believe, however, that much of this flux difference can be explained by error in the accumulation map. There is high accumulation along the west coast on the other side of the ridge (Figure 1) that forms the southern border of the Humboldt drainage. As there are a large number of accumulation measurements for the west coast relative to the Humboldt/Petermann/Ryder drainage, it is likely that in the north the accumulation map is biased high by the coastal data, with largest biases in the Humboldt drainage.

A core at the Humboldt camp (Figure 2) was used to estimate the accumulation rate at 0.14 m/yr (Anklin and others, submitted), which is significantly lower than the value of 0.2 m/yr from the accumulation map. Analysis of a shallow core with layers dating from 1976-1994 yielded an accumulation estimate of 0.178 m/yr (K. Steffen, personal communication). While significantly different, both these values support the conclusion that the accumulation map is biased high over at least part of the Humboldt basin.

It is interesting to rescale the basin-wide accumulation estimates by the ratio of the core-derived accumulation rates to the Ohmura and Reeh value at Humboldt camp. With the 0.14 m/yr rate, we obtain a rescaled flux estimate of 5.57 km^3/yr, indicating a negative mass imbalance of 21% of the measured flux. With the shallow-core value of 0.178, the rescaled flux estimate is 7.18 km^3/yr, suggesting a positive imbalance of only 2%, which is well within the error bars of the flux measurement. While we must be careful in extending results from point estimates

over entire drainages, the Humboldt accumulation field appears to be fairly uniform (though poorly sampled) so that these results should provide reasonable bounds on the current mass balance. From this analysis we conclude that above the inland flux gate, the Humboldt is in balance to within plus or minus 20%. Clearly, more work is needed to improve knowledge of accumulation rates in order to draw firmer conclusions about the mass balance of this region.

The estimated flux for the Humboldt coastal profile exceeds the measured flux by 0.60 km^3/yr along the full profile, while along the subsection of the profile the estimated flux is only 0.1 km^3/yr less than the measured value. Although there is reasonable agreement between the estimated and measured values, the results are inconsistent with those from the inland profile, where the estimated fluxes were too high. Since the accumulation between the profiles is relatively small, the ablation model likely contributes to the inconsistency.

The flux for the subsection of the coastal profile is 1.2 km^3/yr less than that of the inland profile. With an estimated accumulation of 0.72 km^3/yr between the profiles, the ablation between profiles required for steady state is 1.92 km^3/yr. This value is only 62% of the 3.09 km^3/yr of ablation predicted using the degree-day model. Because the dynamics of an ice sheet take several hundreds to thousands of years to respond to a change in mass balance (Paterson, 1994), ablation estimates obtained from flux gates are in some sense temporally averaged over this response time. In contrast, the ablation model is based on climatological data from the last few decades. Thus, if both the degree-day and flux-derived ablation estimates are correct, they would indicate a significant and relatively recent increase in ablation on the Humboldt. We believe, however, that the differences can be explained by error from the ablation model.

Fahnestock and others (1993) proposed that radar imagery can be used to discriminate the

various snow facies (Paterson, 1994) encountered on an ice sheet. Under this interpretation, the brightest region in the SAR imagery shown in Figure 2 (i.e., above the solid orange and dashed blue lines) corresponds to the percolation zone, while the slightly darker adjacent region (i.e., between solid orange and solid blue lines) represents the wet-snow zone. The significantly darker region near the coast (i.e., slightly below the solid blue line) comprises the bare and superimposed ice zones. If this interpretation is correct, then the snow line (snow/firn to ice transition) on the Humboldt is at the light-to-dark backscatter transition below the inland profile. This transition is not sharp, making it is difficult to locate. We estimate the "radar snow line" on the Humboldt to be somewhere around 675-725 meters elevation.

We used the accumulation map and degree-day ablation model to estimate the snow line, which is indicated by the solid orange line in Figure 2. The estimated runoff line is shown as a dashed orange line. Rather than coinciding with the radar snow line, the estimated snow line lies much further inland just above the 1000 m contour. Thus, if the snow line indicated by the radar is correct, then the ablation model is overpredicting melt.

There are a number of parameters that affect the amount of melt predicted by the degree-day model. The easiest and most direct parameters to adjust are the degree-day factors. We scaled these values by 0.62, which is the ratio of the ablation determined from the flux gates to that given by the degree-day model, to obtain values of 0.00186 and 0.00496 meters per degree day for snow and ice, respectively. Using these values, we re-estimated the snow (solid blue) and runoff (dashed blue) lines. The position of this new estimate of the snow line agrees much better with the line predicted by the radar imagery, in particular along the southwestern part of the glacier. Furthermore, the runoff line falls a few kilometers above the area where lakes are first visi-

ble in the SAR imagery and coincides with the percolation-to-wet-snow transition whereas the original degree-day estimate placed the runoff line well into the percolation zone.

The snow zones predicted by the radar reflect the pattern of melt over the last few years. When the ablation model is tuned to match the flux-derived ablation estimate, it independently nearly matches the radar-determined snow and runoff lines, supporting the idea that the dynamics of the Humboldt below the inland profile are in or close to within equilibrium with the present-day ablation rates.

Our rescaling of the degree-day factors was completely empirical and without surface temperature comparison. We do not mean to imply that the rescaled values are representative of the true degree-day factors. There are a number of other parameters in the model that can be adjusted with similar effect. For example the snow line predicted by the model depends strongly on the accumulation rate since the model must first expend degree days to melt the annual snow layer using the lower degree-day factor. Our results do suggest that using fixed parameters, the degree-day model is not capable of predicting drainage-basin-scale differences in ablation rates. For instance, the rescaled model places the snow line over ice-free area in the upper right-hand corner of Figure 2, while the original degree-day factors are in much better agreement with the image data. Perhaps the ablation model could be improved by matching the model to the radar snow line around the entire ice sheet. More work would be needed first to establish a physical basis for the parameter adjustment.

The value we measured for the flux across the Petermann profile is 12.4 km^3/yr (Table 2). The corresponding estimated flux is 13.2 km^3/yr, which 6% larger than the measured value. Considering the uncertainty in the accumulation data, these flux values agree relatively well. Thus,

the accumulation region of the Petermann drainage appears to be in balance to within the uncertainty of the accumulation data.

There is no CORDS ice-thickness profile that follows the grounding line. Rignot and others (1997) have estimated thickness at the grounding line using elevation data and making an assumption of hydrostatic equilibrium. They have compared these estimates with longitudinal thickness profiles that cross the grounding line (i.e., the longitudinal profile in Figure 2) and estimated the thickness errors at ±10 %. With these data they estimate the flux at the grounding line to be 12.0 km^3/yr. This value agrees exactly with the estimated flux at the grounding line. As with the Humboldt, however, these data are inconsistent with the data from the upper flux gate.

Starting with the measured flux at the upper profile, then with accumulation between profiles of 0.2 km^3/yr and ablation of 1.43 km^3/yr, the flux at the grounding line should be 11.2 km^3/yr. While these values indicate a negative imbalance of 0.8 km^3/yr, they are well within the ±10 % flux uncertainty due to thickness error. Thus, the region of the Petermann below the CORDS profile, which encompasses most of the ablation area, seems to be in balance to within the limits of the flux measurements.

Even if there were no error in the measured flux, much of the 0.8 km^3/yr difference can be ascribed to causes other than a negative mass balance. First as demonstrated for the Humboldt, the errors in the ablation model can be substantial. The transition from bright to dark in SAR amplitude imagery is extremely subtle for the Petermann so that we are unable to determine the radar snow line with any certainty. Nevertheless, the data suggest that the disparity between the radar snow line and the estimated snow line is at least as great as that observed for the Humboldt. If this is the case, then 0.5 km^3/yr of the 0.8 km^3/yr difference can be explained as overprediction

of melt by the degree-day model. A second contributor to the difference in fluxes is the small amount of inflow (i.e., approximately 0.1-0.3 km^3/yr) from smaller glaciers between the profiles.

We measured the Ryder flux at the transverse profile shown in Figure 3. The estimated flux of 5.37 km^3/yr is 38% greater than the measured value of 3.9 km^3/yr. This difference, which indicates a substantial thickening above the profile, is too large to be explained by error in accumulation data. In all of the above measurements, we have assumed that the flux measured over the period of a few days in the winter can be scaled to determine the annual flux. This is a reasonable assumption for many outlet glaciers, particularly when the flux gate is well inland. We have no evidence of time-varying flow for the Petermann or Humboldt. In fact, Rignot (1996) found good agreement between his estimate of discharge (from 3-day data) and those of Higgins (1991), which were based on velocity measurements made from pairs of photographs separated by many years.

A mini-surge has been observed for the Ryder (Joughin and others, 1996c), where velocities increased by at least a factor of three over much of the glacier, including the area spanned by the CORDS profile. It is not known yet whether this was an isolated event, an episodic event occurring every few years or decades, or a seasonal, melt-related event. The flux data could indicate that the mini-surge is seasonal or perhaps episodic with a relatively frequent recurrence rate. If we apply the factor of thee increase in speed during the surge, then the Ryder would have to be in its mini-surge state for 69 days each year for the flux to match the estimated value of 5.37 km^3/yr. The factor of three is a lower bound on the increase in speed during the mini-surge, so the actual number of days could be lower, perhaps as few a fifteen if the speedup was as much as ten times the normal flow rate. Given the uncertainty in the annual flux measurements, we are

unable to estimate the state of balance for the Ryder with any level of certainty. Our data support the hypothesis that the Ryder is subject to relatively frequent mini-surges. Clearly, to make flux measurements for the Ryder and other glaciers with variable flow we require a method of measurement that yields annually averaged velocity (i.e., feature tracking). Alternatively, the flux gate could be moved further inland, where flow should be more steady.

LONGITUDINAL VELOCITY AND THICKNESS PROFILES

We have CORDS ice-thickness data for the longitudinal profile shown in Figure 2 running down the Petermann. Plots of the ice thickness, bed elevation, surface elevation, and velocity along the profile are shown in Figure 5a. The elevation data were determined interferometrically except for the interval from 150 to 170 km and on the floating ice. KMS data have been substituted for these sections of the profile. Bedrock elevations were obtained by subtracting the CORDS ice-thickness data from the surface-elevation profile. The profile locations in the velocity map (Figure 2) have been marked with dots at 10 km intervals. For reference the distance is given for the first visible dot of each profile (Figure 5).

Several of the bedrock bumps correlate well with features in the elevation profile, in particular for the fast moving region around 190 km. The strong downward spike in the velocity at about 200 km is probably the result of a phase unwrapping error due to the strong motion-related phase gradient on the steep downward face of the corresponding bump in the surface topography. The velocity in the range from 150 to 170 km is not as smooth as for other portions of the profile since we had insufficient SAR data to determine the fine-scale elevation needed to remove artifacts caused by vertical displacement (Joughin and others, 1996b).

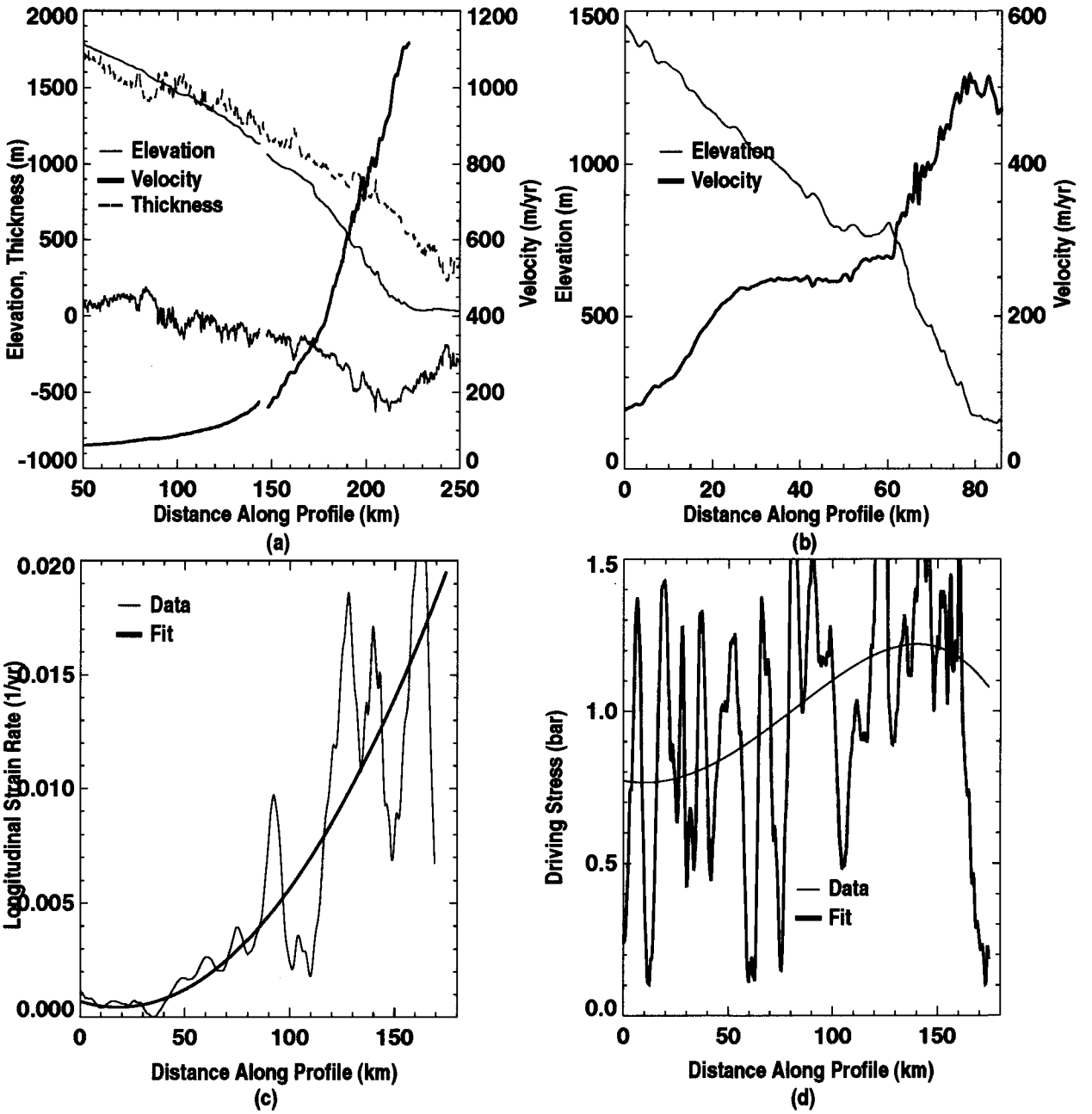

Figure 5. Longitudinal profiles for the Petermann showing (a) velocity, elevation, and thickness along CORDS profiles, (b) velocity and elevation along the central line with bed elevation from extrapolated CORDS profile, (c) centerline strain rate and (d) driving stress. The slope-estimated flow direction and across-track component were used to determine the velocity magnitude.

The speed increases steadily along the profile from 60 m/yr to nearly 1100 m/yr at the grounding line, which is the last point at which we were able to determine the velocity. The increase in speed is moderate along the first section of the profile (i.e., 50-110 km) but then begins to increase much more rapidly. While some of this increase can be attributed to a longitudinal increase in speed, some of the increase occurs where the profile crosses the shear margin, which is one of the disadvantages in studying a profile that does not follow a flow line.

To better study longitudinal variation along the Petermann, we have selected a profile that runs down the center of the glacier, which is shown in yellow in Figure 2. Since we do not have CoRDs data along this profile, we projected the thickness data from the nearby profile onto the centerline profile to get a rough estimate of the bed elevation, which is shown along with the velocity and surface topography in Figure 5b. The extrapolated bed profile has been smoothed to remove small-scale topography that clearly does not reflect the true topography. While there maybe significant errors in this estimate of the bed, we believe that it is more accurate than existing, low-resolution bed DEMs and provides a useful approximation for the following discussion.

The trend in this profile, which is similar to the trend in the original CoRDS profile, has the velocity increasing relatively slowly along the first 50 km of the profile and undergoing a much more rapid increase thereafter. This trend can also be seen in the longitudinal strain rates, which are included in Figure 5c. The strain rates computed by differencing at intervals of 5.33 km exhibit substantial fluctuations over lengths-scales from 10 to 30 km. Some of this variation can be attributed to small-scale errors in the velocity (i.e., from vertical displacement), while some of the variation reflects true variation in the strain rate. To examine the trend in the strain rate data, we fit a third-order polynomial to the velocity field and computed the strain rate from the result.

This results shows that the strain rate increases by an order of magnitude over the length of the profile.

Figure 5d shows plots of driving stress computed directly from the data and from fits to the surface and thickness profiles. Applying these data with a simple laminar flow model (Paterson, 1994), indicates that some sliding must be occurring over the first fifty kilometers of the profile as the velocities of 80 to 120 m/yr cannot be explained entirely by deformation without a layer of temperate ice several hundred meters thick. Model runs for the entire ice sheet by Greve (1997) indicate that the basal ice is at the pressure melting point in this region, indicating the sliding is likely to occur in this region.

The sudden increase in velocity and strain rate correlate well with the region of strong convergence seen in Figure 2. This rapid increase is also evident in the balance velocities, indicating that ice sheet is responding as it must to maintain continuity. It is not clear whether the region of convergence and rapid flow is located where it is because of some geometric control forced by the channel (i.e., a steep headwall) or whether it is determined by some change in the basal hydrology that enhances sliding.

The thickness data from the Ryder longitudinal profile (Figure 3) are plotted in Figure 6a along with the corresponding velocity and elevation data. The profile appears to cross the channel wall at about 40 km, leading to the more than 500-meter drop seen in the bed topography. There is an overdeepened area from 60 to 80 km with what could be a prominent ridge at 85 km. The presence of a ridge in these regions has been inferred from surface features by Joughin and others (1996c). They hypothesized that water could pond behind the ridge until a critical pressure

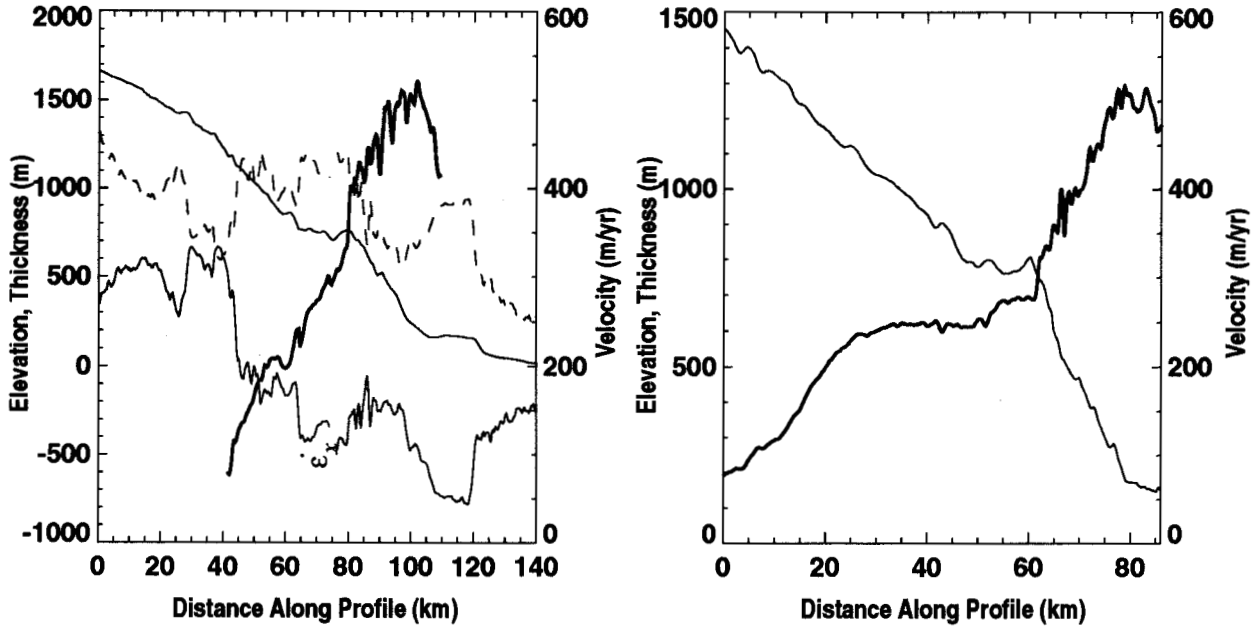

Figure 6 Longitudinal profiles for Ryder showing (a) velocity, elevation, and thickness along CORDS profiles and (b) velocity and elevation along the yellow flowline shown in Figure 3.

was reached, triggering the Ryder mini surge. A similar phenomenon could occur in the even deeper basin just before the grounding line.

The increase in velocity over the basin (i.e., 60 to 80 km) results from the profile cutting across the shear margin. Figure 6b shows data from the yellow flow line in Figure 3 that runs down the Ryder's other branch. In this figure, the ice plain over the basin is located at about 45-60 km with the velocity remaining nearly constant over this feature and all the way back to about 25 km. While this is consistent with the low driving stress over the basin, the strain rates are still low in the region from 20-45 km where the slope is relatively steep. This could indicate a deepening of the channel over this region. The flow also appears divergent over this region (Figure 3) so that a widening of the channel could also explain the leveling of the velocity.

CONCLUSIONS

We have combined remote-sensing data from a number of sources to provide a comprehensive data set for the Humboldt, Ryder and Petermann glaciers. From these data we were able to estimate discharge for these glaciers. The Humboldt and Petermann appear to be in balance to within the level of uncertainty of existing accumulation maps and ablation models. The data for the Ryder are not so easily explained, and may indicate that a significant portion of its discharge occurs when it is in a mini-surge state. The longitudinal profile data has given us an initial look at the dynamics of the Petermann and Ryder.

ACKOWLEDGEMENTS

I. Joughin and R. Kwok performed this work at the Jet Propulsion Laboratory, California Institute of Technology under contract with NASA. Mark Fahnestock was supported under NASA MTPE grant NAGW4285.

We thank S. Ekholm of the National Survey and Cadastre, Copenhagen, Denmark for providing us with the DEM. We also wish to thank C. Werner of the Jet Propulsion Laboratory, California Institute of Technology for providing us with a SAR processor for the raw signal data and E. Rignot of JPL who provided some of the code to implement the degree-day model. Thanks to K. Steffen of University of Colorado for providing us with accumulation and velocity measurements at Humboldt Camp and to Doug MacAyeal of the University of Chicago for discussions regarding polythermal ice.

REFERENCES

Anklin, M., R.C. Bales, E. Mosley-Thompson, and K. Steffen. Annual accumulation at two sites in northwest Greenland during recent centuries. *Journal of Geophysical Research*, submitted.

Alley, R.B. and C. R. Bentley. 1988. Ice-core analysis on the Siple Coast of West Antarctica. *Ann. Glaciol.*, **11**, 1-7.

Bindschadler, R. A. 1984. Jakobshavns Glacier drainage basin: a balance assessment. *J. Geophys. Res.*, **89**(C2), 2066-2072.

Chuah, T., S. Gogineni, C. Allen, and B. Wohletz. 1996. An improved coherent radar depth sounder. RSL Technical Report, TR 10470-4.

Ekholm, S. 1996. A full coverage, high-resolution, topographic model of Greenland, computed from a variety of digital elevation data. *J. Geophys. Res.*, **21**(B10), 961-972.

Fahnestock, M., R. Bindschadler, R. Kwok, and K. Jezek. 1993. Greenland Ice Sheet surface properties and ice dynamics from ERS-1 SAR imagery. *Science*, **262**, 1530-1534.

Ferrigno J. G., B. K. Lucchitta, K. F. Mullins, A. L. Allison, R. J. Allen, and W. G. Gould. 1993. Velocity measurement and changes in position of Thwaites Glacier/iceberg tongue from aerial photography, Landsat images and NOAA AVHRR data. *Ann. Glaciol.*, **17**, 239-244.

Gabriel, A. K., R. M. Goldstein, and H. A. Zebker. 1991. Mapping small elevation changes over large areas: differential radar interferometry. *J. Geophys. Res.*, **94**(B7), 9183-9191.

Goldstein, R. M. 1995. Atmospheric limitations to repeat-track radar interferometry. *Geophys. Res. Lett.*, **22**(18), 2517-2520.

Goldstein, R. M., H. Engelhardt, B. Kamb, and R.M. Frolich. 1993. Satellite radar interferometry for monitoring ice sheet motion: application to an Antarctic ice stream. *Science*, **262**, 1525-1530.

Goldstein, R. M., H. A. Zebker, and C. L. Werner. 1988. Satellite radar interferometry: two-dimensional phase unwrapping. *Radio Science*, **23**(4), 713-720.

Greve, R. 1997. Application of a polythermal three-dimensional ice sheet model to the Greenland Ice Sheet: response to steady-state and transient climate scenarios. *J. Climate*, **10**(5), 901-918.

Hartl P., K. H. Thiel, X. Wu, C. Doake, and J. Sievers. 1994. Application of SAR interferometry with ERS-1 in the Antarctic. *Earth Observation Quarterly*, **43**, 1-4.

Huybrechts, P., A. Letreguilly, N. Reeh. 1991. The Greenland Ice Sheet and greenhouse warming. *Paleo3*, **89**, 399-412.

Higgins, A.K. 1991. North Greenland glacier velocities and calf ice production. *Polarforschung*, **60**(1), 1-23.

Joughin, I. R. 1995. Estimation of ice sheet topography and motion using interferometric synthetic aperture radar. (Ph. D. Thesis, University of Washington)

Joughin, I. R., D. P. Winebrenner, and M. A. Fahnestock. 1995. Observations of ice-sheet motion in Greenland using satellite radar interferometry. *Geophys. Res. Lett.*, **22**(5), 571-574.

Joughin, I., D. Winebrenner, M. Fahnestock, R. Kwok, and W. Krabill. 1996a. Measurement of ice-sheet topography using satellite radar interferometry. *J. Glaciology,* **42**(140), 10-22.

Joughin, I., R. Kwok, and M. Fahnestock. 1996b. Estimation of ice-sheet motion using satellite radar interferometry. *J. Glaciology,* **42**(142), 564-575.

Joughin, I., S. Tulaczyk, M. Fahnestock, and R. Kwok. 1996c. A mini-surge on the Ryder Glacier, Greenland observed via satellite radar interferometry. *Science,* **274**, 1525-1530.

Joughin I., M. Fahnestock, S. Ekholm, and R. Kwok. 1997. Balance Velocities for the Greenland Ice Sheet, *Geophys. Res. Lett.,* **24**(23), 3045-48.

Joughin I., R. Kwok, and M. Fahnestock. In press. Interferometric estimation of three-dimensional ice-flow using ascending and descending passes. *IEEE Trans. Geosci. Rem. Sen.*

Kwok R., M. A. Fahnestock. 1996. Ice sheet motion and topography from radar interferometry. *IEEE Trans. Geosci. Rem. Sen.*, **34**(1), 189-200.

Li, F. K., and R. M. Goldstein. 1990. Studies of multi-baseline spaceborne interferometric synthetic aperture radars. *IEEE Trans. Geosci. Rem. Sen.*, **28**(1), 88-97.

Ohmura, A., and N. Reeh. 1991. New precipitation and accumulation maps for Greenland. *J. Glaciology,* **37**(125), 140-148.

Paterson, W. S. B. 1994. *The Physics of Glaciers.* 3rd Ed. Oxford: Pergammon Press.

Raju, G., W. Xin, and R. K. Moore. 1990. Design, development, field observations, and preliminary results of the coherent Antarctic radar depth sounder (CARDS) of the University of Kansas, U.S.A. *J. Glaciology,* **36**(123), 247-254.

Reeh, N. 1989. Parameterization of the melt rate and surface temperature on the Greenland Ice Sheet. *Polarforschung*, **59**(3), 113-128.

Rignot, E., K. C. Jezek, and H. G. Sohn. 1995. Ice flow dynamics of the Greenland ice sheet from SAR interferometry. *Geophysical Research Letters*, **22**(5), 575-578.

Rignot, E., 1996., "Tidal flexure, ice velocities, and ablation rates of Petermann Gletscher, Greenland," *J. of Glaciology,* **42**(142), 476-485.

Rignot, E. J., S. P. Gogineni, W. B. Krabill, and S. Ekholm. 1997. North and northeast Greenland ice discharge from satellite radar interferometry. *Science*, **276**, 934-937.

Rignot, E. Personal communication. 1997.

Scambos, T. A., M. J. Dutkiewicz, J. C. Wilson, and R. A. Bindschadler. 1992. Application of image cross-correlation to the measurement of glacier velocity using satellite image data. *Rem. Sens. of the Environment*, **42**, 177-186.

Steffen, K. 1997. Personal communication.

Zebker, H. A., C. L. Werner, P. A. Rosen, and S. Hensley. 1994. Accuracy of topographic maps derived from ERS-1 interferometric radar. *IEEE Trans. Geosci. Rem. Sen.*, **32**(4), 823-836.